Editors' Suggestion

Luminescence Analysis of Charge-Carrier Separation and Internal Series-Resistance Losses in $Cu(In,Ga)Se_2$ Solar Cells

Uwe Rau,* Vito Huhn, and Bart E. Pieters
IEK5-Photovoltaik, Forschungszentrum Jülich, 52425 Jülich, Germany

(Received 27 February 2019; revised 6 October 2019; accepted 27 May 2020; published 16 July 2020)

$Cu(In,Ga)Se_2$ solar cells are investigated by luminescence measurements. We construct the current versus internal voltage characteristics of these devices from the luminescence intensity at different voltage and light bias conditions. A comparison of these characteristics to electrically measured current versus voltage curves unveils an internal resistance loss that is strongly dependent on voltage bias and illumination. In particular, we find significant residual luminescence for the device under short-circuit conditions. Numerical device simulations reveal that this effect is caused by a drop of the electron quasi-Fermi-level within the space charge region of the absorber material. We use a modified equivalent circuit model to describe the observed behavior in terms of simple equations. We show that such a voltage-dependent series resistance leads to a violation of a linear-network theorem, which under standard circumstances provides a useful method for the determination of the photocurrent collection efficiency. An analysis of resistive and recombination losses in the devices demonstrates that the internal voltage-dependent series resistance causes an efficiency loss of about 1.3% (absolute) for a device with an efficiency 13.4%. Finally, we show that the observed behavior is a general feature of charge-carrier separation in solar cells with finite charge-carrier mobility and that the intensity of the residual short-circuit luminescence provides valuable information on the efficiency of this process.

DOI: 10.1103/PhysRevApplied.14.014046

I. INTRODUCTION

The collection of the photogenerated charge carriers, electrons, and holes, at two different contacts lies in the heart of the photovoltaic action of any solar cell. Perfect carrier collection implies that every electron-hole pair contributes to the short-circuit current. This in turn, is only possible if under short-circuit conditions the concentration of excess carriers in the solar cell is virtually zero because otherwise some of the charge carriers will be lost by radiative recombination [1]. Thus, in a perfect solar cell, as described in the Shockley-Queisser model [2], we can switch off any luminescence by putting the terminal voltage of an illuminated solar cell to zero. Inversely, the detection of photoluminescence from a solar cell under short-circuit conditions is directly indicative of a departure from the ideal case and, consequently, for an efficiency loss. Electro and photoluminescence analysis [3–9] of solar cells is based on the intimate connection between luminescent and photovoltaic material properties as expressed by the optoelectronic reciprocity theorem [10] and by the generalized Planck law [11]. In most cases, luminescence experiments are conducted either under voltage bias (electroluminescence) or by using uncontacted samples, which corresponds to open-circuit conditions (photoluminescence). For crystalline silicon solar cells, photoluminescence under short-circuit conditions was reported by Abbott *et al.* [12] as well as by Hinken and co-workers [13] who determined the effective diffusion length in crystalline Si solar cells from the difference between photoluminescence under open-circuit and that under short-circuit conditions. Juhl and Trupke [14] discussed the luminescence generated by "voltage-independent charge carriers" in the context of implied open-circuit voltages determined by photoluminescence measurements. Finally, it was shown that the luminescence of a solar cell is the superposition of a contribution driven by the external voltage and the luminescence under short circuit [15].

The present paper investigates the photoluminescence of industrially produced $Cu(In,Ga)Se_2$ solar cells under variations of the external voltage bias down to short-circuit conditions. Like in the case of crystalline Si solar cells, we find a significant luminescence intensity under a short circuit. However, in the Si solar cells this residual luminescence stems from diffusion limitations in the very thick quasineutral zone of the absorber [12–14], whereas in the present $Cu(In,Ga)Se_2$ solar cells the luminescence is a result of an *internal* series resistance across the space-charge region (SCR) of the device. The investigation of an internal series resistance goes beyond earlier investigations that were restricted to *external* series-resistance effects,

*u.rau@fz-juelich.de

like the sheet resistance of the emitter of silicon-wafer solar cells [16–18] or window layers of thin-film solar cells [19–22].

The internal series resistance in the $Cu(In,Ga)Se_2$ solar cells under investigation turns out to be strongly dependent on voltage bias. Note that effects from an internal series resistance have been investigated earlier by experiments on *p-i-n* cells, solar cells made from microcrystalline Si [23], and from organic semiconductors [24]. In contrast to these models based on a *p-i-n*-type device structure, the present results are explained in terms of the *p-n*-type junction present in the $Cu(In,Ga)Se_2$ solar cell. For an analytical expression describing this behavior we solve the drift-diffusion equation for minority carriers in the SCR of the cell under light and/or voltage bias. This solution turns out to be compatible with an equivalent circuit model for the solar cell recently introduced by Breitenstein [25,26]. Our experimental results agree well with the theoretical description by the equivalent circuit model as well as with more detailed numerical simulations. We finally discuss the importance of our findings in view of the general mechanisms of charge-carrier collection in solar cells and, especially, with respect to the network theorem of Wong and Green [27] that is the basis of the photocurrent collection method for the analysis of resistive and recombination losses in solar cells [28–32].

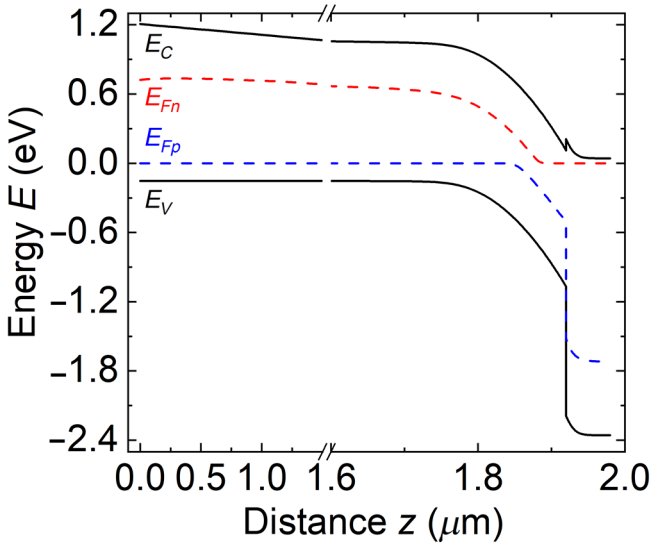

FIG. 1. Band diagram of a graded $CdS/Cu(In,Ga)Se_2$ heterojunction solar cell under external short circuit and under illumination from the right-hand side, as calculated numerically (SCAPS). The significant split of the quasi-Fermi-levels E_{Fn} and E_{Fp} of electrons and holes in the $Cu(In,Ga)Se_2$ absorber is clearly visible. The $Cu(In,Ga)Se_2$ absorber has a significant Ga grading towards the back contact (left) leading to a gradient in the conduction-band energy E_C.

II. THEORY

A. Quasi-Fermi-levels in the space-charge region

Figure 1 shows the band diagram of a $ZnO/CdS/Cu(In,Ga)Se_2$ heterojunction solar cell under illumination and at an external short circuit. It is clearly visible that a considerable split between the electron quasi-Fermi-level (QFL) E_{Fn} and the hole QFL E_{Fp} exists in the SCR as well as in the neutral region of the device. Therefore, also the concentrations n of electrons and the concentration p of holes deviate considerably from their equilibrium values n_0 and p_0, respectively. In the bulk of the device up to half way through the SCR, we have $E_{Fn} > 0$ and for the second half of the SCR and beyond $E_{Fp} < 0$. In the following we derive an analytical solution for the minority carrier (electron) QFL through the SCR under light and/or voltage bias.

The electron current density J_n in the SCR is assumed to be constant. The electron current density is defined by the concentration of electrons and the gradient of the electron QFL according to [33]

$$J_n = -\mu_n n(z)\frac{dE_{Fn}(z)}{dz} = -\mu_n N_C \exp\left[\frac{E_{Fn}(z) - E_C(z)}{kT}\right]\frac{dE_{Fn}(z)}{dz}, \quad (1)$$

where μ_n denotes the electron mobility, N_C the effective density of states in the conduction band, E_C the energy of the conduction band, and kT the thermal energy. With constant J_n and a given dependence of the conduction-band energy on the spatial coordinate z, Eq. (1) is a differential equation for E_{Fn}. Let us assume that the zero of the coordinate system (for energy E and coordinate z) is at the edge of the SCR such that in the depletion approximation the energy of the conduction band follows

$$E_C(z) = E_C(0) - \frac{q^2 N_A}{2\varepsilon_s} z^2 = E_C(0) - az^2. \quad (2)$$

With this approximation we find that the solution of Eq. (1) is given by

$$E_{Fn}(z) = kT\log\left\{\exp\left[\frac{E_{Fn}(0)}{kT}\right] - \frac{J_n}{2\mu_n N_C kT}\exp\left[\frac{E_C(0)}{kT}\right]\frac{\sqrt{\pi}\,\mathrm{erf}\left(z\sqrt{a/kT}\right)}{\sqrt{a/kT}}\right\}. \quad (3)$$

Resolving Eq. (3) for the electron current density and for the boundary conditions at $z = 0$ and $z = w$ yields

$$J_n = \mu_n N_C kT \exp\left[\frac{-E_C(0)}{kT}\right] \frac{2\sqrt{a/kT}}{\sqrt{\pi}\,\mathrm{erf}(w\sqrt{a/kT})} \times \left\{\exp\left[\frac{E_{Fn}(0)}{kT}\right] - \exp\left[\frac{E_{Fn}(w)}{kT}\right]\right\}, \quad (4)$$

where w denotes the width of the SCR. With Eq. (4) the current through the SCR is determined by the values of the electron QFL at the two edges of the SCR. As shown in Fig. 2, we use the equilibrium Fermi energy E_F^0 to define the external voltage via $qV_{\mathrm{ext}} = E_{Fn}(w) - E_F^0$. Accordingly, we replace the electron QFL $E_{Fn}(0)$ by an internal voltage $qV_{\mathrm{int}} = E_{Fn}(0) - E_F^0$. With this Eq. (4) becomes

$$J_n = \mu_n N_C kT \exp\left[\frac{E_F^0 - E_C(0)}{kT}\right] \frac{2\sqrt{a/kT}}{\sqrt{\pi}\,\mathrm{erf}(w\sqrt{a/kT})} \times \left[\exp\left(\frac{qV_{\mathrm{int}}}{kT}\right) - \exp\left(\frac{qV_{\mathrm{ext}}}{kT}\right)\right]. \quad (5)$$

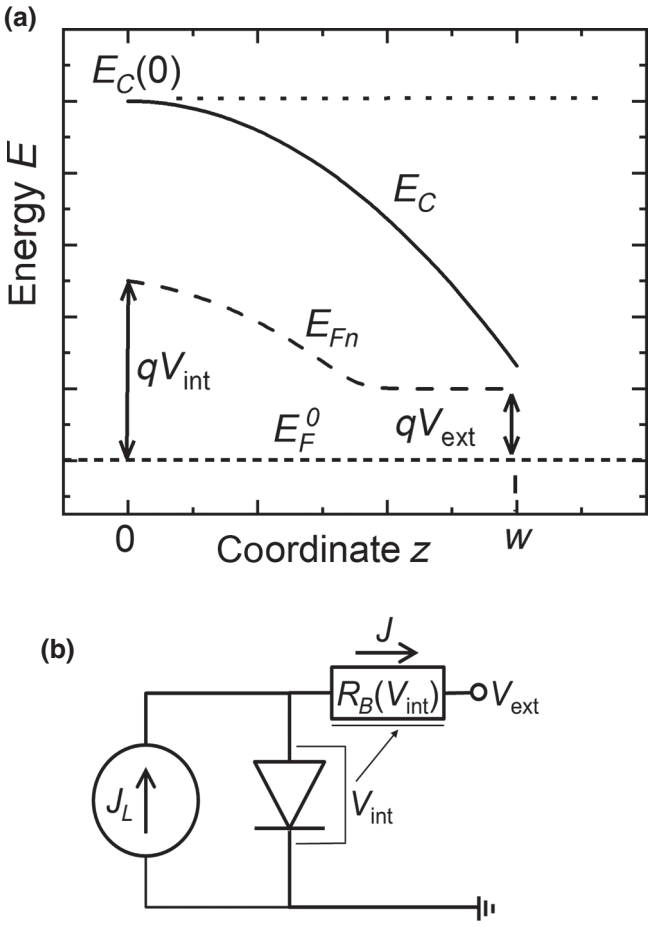

FIG. 2. (a) Definitions underlying the calculation of the electron quasi-Fermi-level E_{Fn} through the space-charge region of a p-n junction with width w and with a parabolic shape of the conduction-band energy E_C. The internal voltage V_{int} is defined as the difference $qV_{\mathrm{int}} = E_{Fn}(0) - E_F^0$ between the electron quasi-Fermi-level $E_{Fn}(0)$ at the edge of the SCR ($z = 0$). The external voltage is defined via $qV_{\mathrm{ext}} = E_{Fn}(w) - E_F^0$. (b) The internal series resistance of the SCR resulting from the shape of $E_{Fn}(z)$ depends on the internal voltage V_{int} as described by a modified equivalent circuit model [25,26].

Because of $qV_{\mathrm{bi}} = aw^2$, the argument of the error function (erf) in Eq. (5) may be expressed via the built-in potential V_{bi}, i.e., $w\sqrt{a/kT} = qV_{bi}/kT$. Likewise, we may use the Debye length $L_D = (\varepsilon_s kT/q^2 N_A)^{1/2} = (kT/2a)^{1/2}$ [33] to write

$$J_n = \sigma_n^0 \frac{kT}{q} \frac{\sqrt{2}/L_D}{\sqrt{\pi}\,\mathrm{erf}(w/\sqrt{2}L_D)} \left[\exp\left(\frac{qV_{\mathrm{int}}}{kT}\right) - \exp\left(\frac{qV_{\mathrm{ext}}}{kT}\right)\right] \quad (6)$$

using the equilibrium conductivity σ_n^0 for electrons in the neutral region. If we have $V_{\mathrm{bi}} >\sim 2kT/q$ or $w >\sim 3L_D$ the error function approaches unity and Eq. (6) simplifies to

$$J_n \approx \sigma_n^0 \sqrt{\frac{2}{\pi}} \frac{kT/q}{L_D} \left[\exp\left(\frac{qV_{\mathrm{int}}}{kT}\right) - \exp\left(\frac{qV_{\mathrm{ext}}}{kT}\right)\right] = J_B \left[\exp\left(\frac{qV_{\mathrm{ext}}}{kT}\right) - \exp\left(\frac{qV_{\mathrm{int}}}{kT}\right)\right] \quad (7)$$

with a prefactor J_B in the second line that is independent of the internal and external voltage. Note that Eq. (7) corresponds to Eq. (2) derived by Breitenstein in Ref. [26] by a more phenomenological approach. We emphasize that Eq. (7) connects the two basic functionalities of a semiconductor junction in a solar cell: (i) the building of an external electrostatic potential V_{ext} as a result of the photogenerated nonequilibrium chemical potential of the charge carriers (expressed by the internal voltage V_{int}) and (ii) the loss of free energy during the collection of these free carriers. Furthermore, the current density J_n cannot be expressed as a function of the difference between V_{ext} and V_{int}. Rather J_n depends on a reference energy for both potentials, the equilibrium Fermi level. One possibility to handle this issue within an equivalent circuit model is to define a resistance that is dependent on one of the two voltages [see Fig. 2(b)] as proposed by Breitenstein [25,26].

B. Internal series resistance and residual short-circuit luminescence

The equivalent circuit shown in Fig. 2(b) contains a voltage-dependent series resistance $R_B(V_{\mathrm{int}})$ in addition to the usual current source for the photogenerated current density J_L and the recombination diode with the diode ideality factor n_{id} and a saturation current density J_0. By

setting the collected current density J_n equal to the internal recombination current density we obtain

$$J_B\left[\exp\left(\frac{qV_{\rm int}}{kT}\right)-\exp\left(\frac{qV_{\rm ext}}{kT}\right)\right] = J_L - J_0\left[\exp\left(\frac{qV_{\rm int}}{n_{\rm id}kT}\right)-1\right]. \tag{8}$$

An analytical treatment of Eq. (8) is possible if the ideality factor on the right-hand side is $n_{\rm id}=1$. Then, resolving Eq. (8) for the internal voltage yields the dependency of the internal on the external voltage yields

$$V_{\rm int} = \frac{kT}{q}\log\left[\frac{J_B}{J_B+J_0}\exp\left(\frac{qV_{\rm ext}}{kT}\right)+\frac{J_L+J_0}{J_B+J_0}\right]. \tag{9}$$

Equation (9) predicts for $V_{\rm ext}=0$ a residual short-circuit value for the internal voltage

$$V_{\rm int}^{\rm SC} = \frac{kT}{q}\log\left[\frac{J_B+J_L+J_0}{J_B+J_0}\right]. \tag{10}$$

Substituting $V_{\rm int}$ in Eq. (8) by Eq. (9) yields for the current voltage (J-V) curve of the entire equivalent circuit

$$\begin{aligned} J &= J_L - J_0\left[\exp\left(\frac{qV_{\rm int}}{kT}\right)-1\right] \\ &= \frac{J_B}{J_0+J_B}\left\{J_L - J_0\left[\exp\left(\frac{qV_{\rm ext}}{kT}\right)-1\right]\right\}, \end{aligned} \tag{11}$$

i.e., the $J(V_{\rm ext})$ curve is a compressed version of the $J(V_{\rm int})$ curve. This implies that the short-circuit current density $J_{\rm SC}$ is reduced with respect to the photogenerated current density J_L by a factor $J_B/(J_0+J_B)$. Note that with $J_L \gg J_0$ the present Eqs. (9) and (11) correspond to Eqs. (9) and (10) in Ref. [25].

The internal series resistance R_B can be finally expressed either as a function of the internal voltage or the external voltage via

$$\begin{aligned} R_B &:= \frac{V_{\rm int}-V_{\rm ext}}{J} \\ &= \frac{V_{\rm int} - \frac{kT}{q}\log\left[\frac{J_B+J_0}{J_B}\exp\left(\frac{qV_{\rm int}}{kT}\right)-\frac{J_L+J_0}{J_B}\right]}{J_L - J_0\left[\exp\left(\frac{qV_{\rm int}}{kT}\right)-1\right]} \\ &= \frac{J_B+J_0}{J_0}\frac{\frac{kT}{q}\log\left[\frac{J_B}{J_B+J_0}\exp\left(\frac{qV_{\rm ext}}{kT}\right)+\frac{J_L+J_0}{J_B+J_0}\right]-V_{\rm ext}}{J_L - J_0\left[\exp\left(\frac{qV_{\rm ext}}{kT}\right)-1\right]}. \end{aligned} \tag{12}$$

We note that the dependence of the internal series resistance on the internal voltage $V_{\rm int}$ as derived here for a p-n junction is different from the results obtained earlier for p-i-n junctions [23,24], which reads

$$R_{\rm int} = R_0\exp\left(\frac{-qV_{\rm int}}{kT}\right). \tag{13}$$

In the following we compare our experimental results with both approaches, i.e., the model derived here in Eq. (12) and the p-i-n model in Eq. (13).

III. EXPERIMENTAL RESULTS AND DISCUSSION

A. Experimental setup and numerical simulation method

For our experiments, we use industrially prepared ZnO/CdS/Cu(In,Ga)Se_2 solar cells prepared by co-evaporation [34]. The cells of size 1.6×0.4 cm^2 are positioned on a 10×10 cm^2 large substrate, which is cut from industrially produced modules. The cells are mounted into a luminescence imaging setup as described in Refs. [31,32] that allows the homogeneous irradiation of the sample with a 808-nm laser. The laser intensity is adjusted such that the short-circuit current density of the sample closely matches its short-circuit current density under AM 1.5 G conditions (at AM 1.5 G: $J_{\rm SC}^{\rm AM1.5}=29.2$ mA/cm^2; at PL setup: $J_{\rm SC}^{\rm PLsetup}=30.98$ mA/cm^2). In Table I we summarize the solar-cell properties as measured under various conditions. Within the setup current-voltage (I-V) characteristics are measured in the dark and under illumination while simultaneously taking luminescence images. The only correction applied to the images is a subtraction of a background image where the applied voltage to the sample is zero and the illumination is turned off.

For the numerical simulations we use the numerical device simulator solar cell capacitance simulator (SCAPS) [35], which is especially suited to describe solar cells based on Cu(In,Ga)Se_2. The set of material parameters entering in our simulations is based on that used in Refs. [36,37]. We adapt this parameter set to our actual device (e.g., by including a heavy Ga grading) and to fit our experimental results. These modifications are documented in the Supplemental Material to the present paper [38].

TABLE I. Solar-cell parameters under various conditions. In the table the solar-cell parameters under AM.15 G spectrum, 808-nm monochromatic laser light and 808-nm laser light corrected to the AM1.5 G short-circuit current density. Note that the efficiency under 808 nm (*) is computed assuming an incoming power of a 1000 W/m^2, such that the value can be compared to the AM1.5 G spectrum value.

	$J_{\rm SC}$ (mA/cm^2)	$V_{\rm OC}$ (V)	FF (%)	η (%)
AM 1.5 G	29.2	0.713	65	13.5
808 nm	31.0	0.710	64	14.0*
808 nm corrected	29.2	0.710	64	13.4

B. Luminescence results

Figures 3(a)–3(d) shows a series of luminescence pictures of a Cu(In,Ga)Se_2 solar cell and illumination and at different external voltages. The signal of these pictures is then integrated over the entire cell area to yield a single value for the luminescence per picture. From this signal S_{em} the internal voltage V_{int} is determined with

$$V_{int} = \frac{kT}{q}\log(S_{em}) + V_{offs}. \tag{14}$$

We eliminate the unknown offset voltage V_{offs} (which is the same for all pictures) by scaling the value at the open circuit in a way that $V_{int,OC} = V_{ext,OC}$ [39]. Herewith, we obtain the absolute values for V_{int} under all external bias conditions as depicted by the $V_{int}(V_{ext})$ curve in Fig. 4. Since the current through the device is externally measured for each bias point we are able to deduce a current versus internal voltage $J(V_{int})$ curve of the device as shown in Fig. 3(e).

Figure 3(e) shows the J-V characteristics measured in the dark and under illumination ($J_{SC}^{lum} = 31.0\,mA\,cm^{-2}$). Also shown are both current versus internal voltage $J(V_{int})$ curves. With respect to the externally measured curves, the dark $J(V_{int})$ curve is shifted towards higher voltages and the illuminated $J(V_{int})$ towards lower voltages. From the difference $V_{ext} - V_{int}$ at a given current density J the total series resistance as determined from the experiment is calculated via

$$R_S = \frac{V_{ext} - V_{int}}{J}. \tag{15}$$

Figure 5 displays the dependence of the series resistance R_S for the dark and the illuminated case on the external [Fig. 5(a)] and on the internal voltage [Fig. 5(b)].

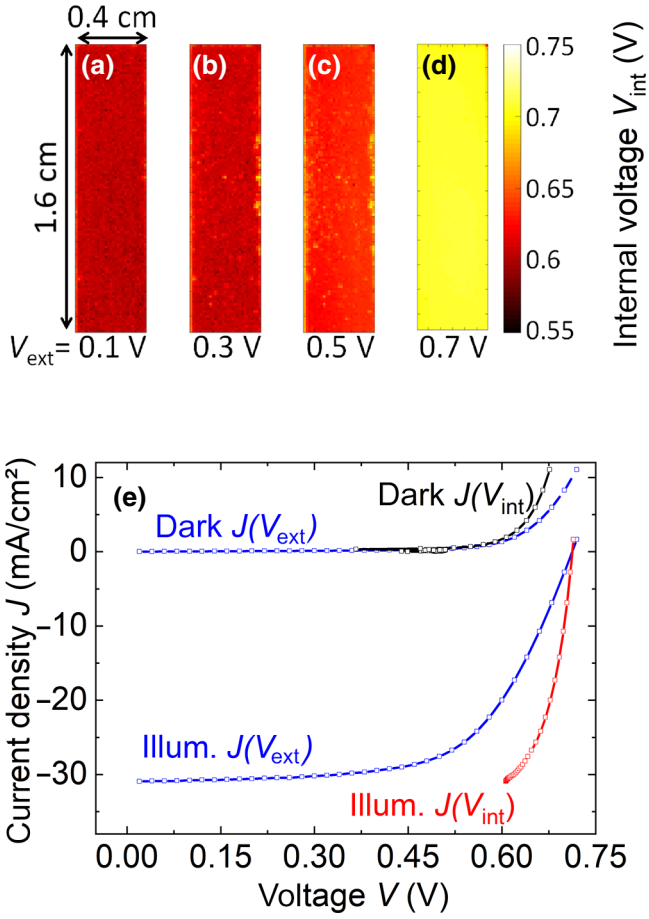

FIG. 3. (a)–(d) Experimentally determined internal voltage maps at various external voltages calculated from luminescence images under illumination. It is visible that even at low external voltages, still a significant amount of luminescence is seen, which shows a large internal voltage. The sample looks homogenous, which allows the use of the average across the sample. (e) J/V and J/V_{int} characteristics, which are determined simultaneously by taking luminescence images during the J/V sweep once in the dark and once under illumination. The internal voltages are larger than the external voltages when the current is negative and vice versa. In particular, at short circuit under illumination the internal voltage is much larger than the external voltage.

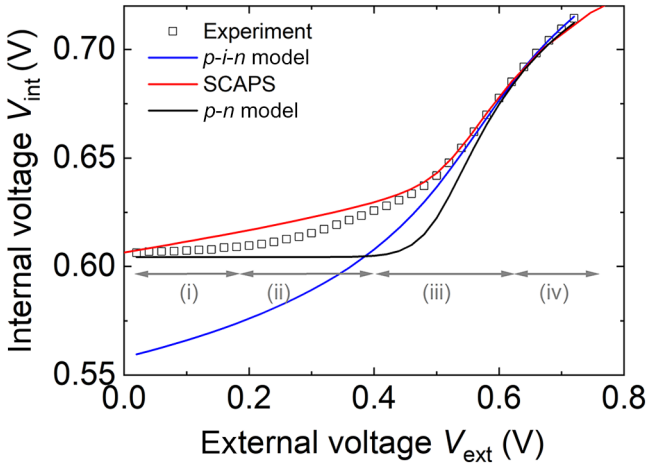

FIG. 4. Internal voltages V_{int} as determined from luminescence images via Eq. (14) as a function of the externally applied voltage V_{ext} (open symbols). The full red line corresponds to numerical simulations via SCAPS using the parameter set given in the Supplemental Material [38]. The black line is obtained from the p-n model described in Sec. II using $J_B = 2.5 \times 10^{-9}\,mA\,cm^{-2}$, $J_0 = 2.45 \times 10^{-8}\,mA\,cm^{-2}$, $J_L = 32.5\,mA\,cm^{-2}$, $n_{id} = 1.3$, and $R_{ext} = 3.5\,\Omega\,cm^2$. The blue line represents the p-i-n model [Eq. (13)] with $R_0 = 6.9 \times 10^7\,\Omega\,cm^2$ and $R_{ext} = 3.26\,\Omega\,cm^2$. The voltage ranges (i)–(iv) represent (i) a saturation at a constant value of the experimental V_{int} values at $V_{int} \approx V_{int}^{SC}$ towards lower voltages [$0 \le V_{ext} < 0.2$ V], (ii) a slight leveling off in the range $0.2\,V \le V_{ext} \le 0.5\,V$, (iii) a steep increase of V_{int} for $0.5\,V \le V_{ext} \le 0.65\,V$, and (iv) a bending over in the range $0.65\,V \le V_{ext}$ due to the external series resistance.

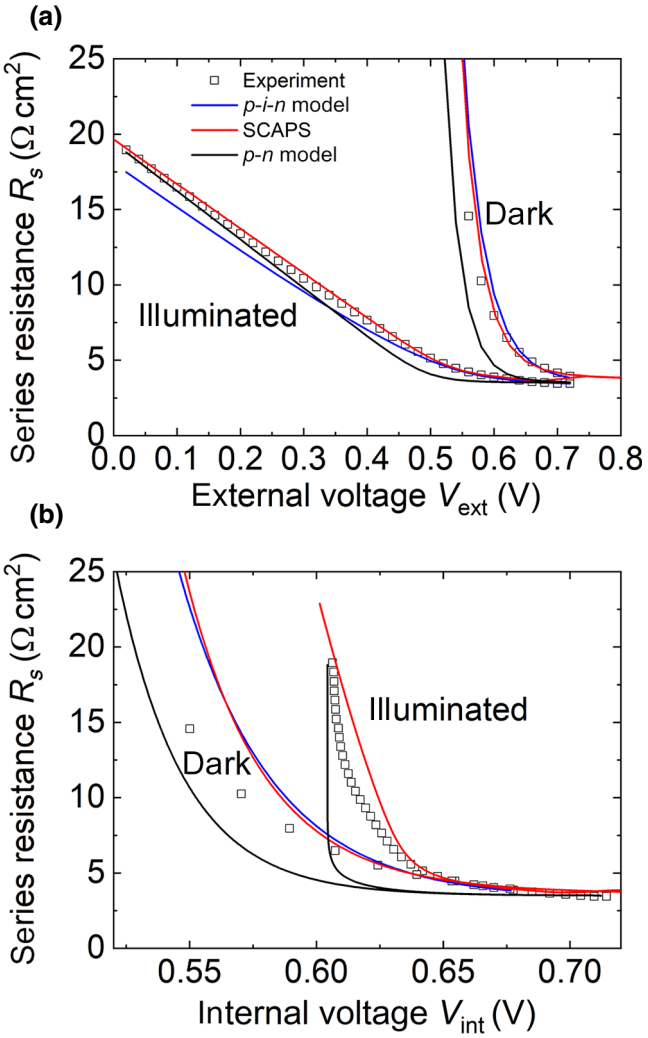

FIG. 5. Series resistance determined from the difference of the internal and external voltage according to Eq. (15) plotted as a function of the external (a) and internal (b) voltage. All models reproduce the characteristic behavior of the series resistance when plotted against the external voltage, which is seen in the experiment. In the dark an exponentially increasing series resistance towards low voltages is seen, which changes to become linearly increasing under illumination. When plotted against the internal voltage the differences between the models become more significant. The *p-i-n* model cannot reproduce the different behavior seen in the experiment under illumination and in the dark as it only depends directly on the internal voltage. The SCAPS model reproduces the experimental result under illumination especially at voltages larger than 0.63 V well, but it fails to show the singularity seen in the experiment under illumination. This abrupt rise is best reproduced by the *p-n* model.

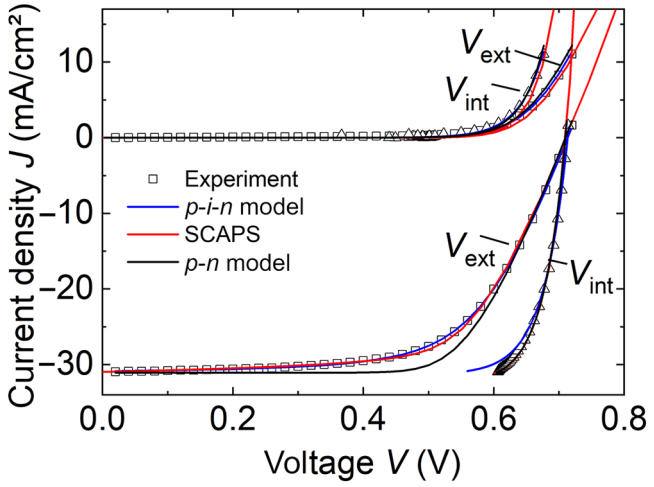

FIG. 6. Experimentally and modeled J-V and J-V_{int} characteristics in the dark (top) and under illumination (bottom). The J-V_{int} characteristics show larger voltages when the current flow is negative and lower voltages when the current flow is positive. The different models are fitted to the experimentally determined J-V characteristic and all models reproduce the characteristics well. The most significant deviation is seen between the fitted *p-n* model and the J-V characteristic determined under illumination. The *p-n* model does not have the ability to introduce a significant gradient to the illuminated J-V characteristic at voltages below 0.4 V. This is better reproduced with the SCAPS model, where the gradient can be adjusted by the electron mobility in the bulk, and the *p-i-n* model.

C. Comparison to model and device simulations

In the following, we compare our experimental results to the model outlined in Sec. II where we use a numerical solution of Eq. (8) for the case of nonideal recombination ($n_{id} \neq 1$). In a next step we perform numerical device simulations using SCAPS with the parameter set given in the Supplemental Material [38]. The aim of the fitting procedure is to reproduce simultaneously the $V_{int}(V_{ext})$ curves (Fig. 4), the $R_S(V_{ext})$ [Fig. 5(a)], the $R_S(V_{int})$ [Fig. 5(b)], as well as the external $J(V_{ext})$ and internal current versus voltage $J(V_{int})$ curves, as shown in Fig. 6.

Note that in the case $J_L \gg J_B \gg J_0$ the residual short-circuit internal voltage given in Eq. (10) reduces to

$$V_{int}^{SC} \approx \frac{kT}{q} \log\left(\frac{J_L}{J_B}\right). \tag{16}$$

This approximation is valid also for the nonideal recombination situation ($n_{id} \neq 1$) as shown in Appendix A. With Eq. (16), J_B is essentially fixed by the experimental value of V_{int}^{SC} for the semianalytical approach using Eq. (8). We use $J_B = 2.5 \times 10^{-9}$ mA cm^{-2} to reproduce an asymptotic value $V_{int}^{SC} \approx 604$ mV as shown in Fig. 4. A good simultaneous fit of the illuminated and dark J-V characteristics (as shown in Fig. 6) requires an ideality factor $n_{id} = 1.3$. The saturation current density J_0 is adjusted to yield the experimental open-circuit voltage $V_{OC} = 710$ mV with a photogenerated current density $J_L = 32.5$ mA cm^{-2}. Note

that the measured short-circuit current is reduced by

$$\Delta J_{SC} = J_L - J_{SC} \approx J_0 \left(\frac{J_L}{J_B}\right)^{\frac{1}{n_{id}}}. \quad (17)$$

The approximate value is obtained from Eq. (11) for $J_L \gg J_B \gg J_0$. In Appendix A we show that Eq. (17) is also a good approximation for $n_{id} \neq 1$. Finally an external series resistance $R_{ext} = 3.5\,\Omega\text{cm}^2$ is added such that the total series resistance adds up to $R_S = R_B + R_{ext}$, where R_S denotes the *experimental* value from Eq. (15) and R_B the *theoretical* value from Eq. (12). Note that this relatively high value of the external series resistance R_{ext} is on the one hand due to the relatively low conductivity of the ZnO window layer in industrial solar cells and on the other hand to the experimental contacting scheme used in this work.

With these assumptions, we can reproduce the overall behavior of the $R_S(V_{ext})$ and $R_S(V_{int})$ curves in Fig. 5, the $V_{int}(V_{ext})$ curve shown in Fig. 4, as well as the external and internal current versus voltage curves in Fig. 6. For completeness, we also include the simpler dependency of the internal series resistance R_{int} on the internal voltage V_{int} according to Refs. [23,24] as expressed by Eq. (13) and refer to this approach as the *p-i-n* model, in contrast to the *p-n* model as given by Breitenstein [25,26] and derived in Sec. II.

Within the SCAPS simulations, the internal voltage V_{int} is determined from the product of the electron and hole densities and calibrated by the external voltage at open-circuit conditions, in analogy to the experiment. For the adaption of parameters within the numerical device simulations, we bear in mind that in Eq. (7), we have the proportionality $J_B \propto \sigma_{n0}/L_D \propto \mu_n/\sqrt{N_A}$. Thus, a lowering of J_B and the consequent increase of V_{int}^{SC} results both from reducing μ_n as well as from increasing N_A. Thus, to fit the experimental results, the doping and the electron mobility is manually adjusted to be able to reproduce on the one hand the dependence of the internal voltage on the external voltage (by lowering the doping density to $N_A = 2.1 \times 10^{15}\ \text{cm}^{-3}$) and, on the other hand, the current versus external voltage at low voltages under illumination (by lowering the electron mobility to $\mu_n = 3\,\text{cm}^2\,\text{V}^{-1}\,\text{s}^{-1}$). In the end the illumination intensity had to be adjusted slightly to 540 Wm^{-2} to fit the short-circuit current of *J-V* characteristic. The final fit is shown in Fig. 6 together with the experimental results. The other parameters are kept equal to the one in Table I (Supplemental Material [38]).

The relatively low value for the electron mobility ($\mu_n = \mu_n = 3\,\text{cm}^2\,\text{V}^{-1}\,\text{s}^{-1}$) is most likely a result of band-gap fluctuations or potential fluctuations [40] in the Cu(In,Ga)Se_2 absorber. On the one hand, there is increasing experimental evidence for these fluctuations [41–43]. On the other hand, such fluctuations provide internal barriers for the transport of both types of carriers [40]. Thus, especially the (effective) minority carrier mobility may considerably fluctuate across the absorber on length scales that are not resolved by the present luminescence measurements. Because of the nonlinear dependence of our measurements on μ_n as given by Eq. (17), the observed behavior could be over proportionally determined by effective low-mobility regions.

In the following, we discuss the predictions of two models (*p-n* and *p-i-n*) and the result of the numerical device simulation in comparison to the experimental result. Figure 4 demonstrates that the SCAPS simulation (red line) reproduces most details of the experimental result (open symbols): (i) a saturation of $V_{int} \approx V_{int}^{SC}$ towards $V_{ext} = 0\,\text{V}$, (ii) a slight increase of V_{int} in the range $0.2\,\text{V} \leq V_{ext} \leq 0.5\,\text{V}$, (iii) a steep increase for $0.5\,\text{V} \leq V_{ext} \leq 0.65\,\text{V}$, and finally (iv) a bending over in the range $0.65\,\text{V} \leq V_{ext}$. Three of these four features are also reproduced by the *p-n* model (black line) only the transition between the low-voltage saturation (i) and the steep increase (iii) is rather abrupt, essentially leaving out the transition regime (ii). Notably, the experimental curve in the saturation region (i) is even better reproduced by the analytical model as compared to the SCAPS simulations. The *p-i-n* model accurately reproduces the high-voltage regions (iii) and (iv) but fails entirely to describe the saturation and finite internal voltages towards lower external voltages.

The dependency of the series resistance on the external voltage V_{ext} [Fig. 5(a)] is well described by all three approaches, the *p-n* and the *p-i-n* model as well as by the numerical simulations. All approaches yield a significant difference between the series resistance in the dark and under illumination, where R_S saturates at approximately the value of the external series resistance $R_{ext} = 3.5\,\Omega\,\text{cm}^2$ for high voltages.

A much steeper increase of R_S in the dark towards lower voltages as compared to the increase of R_S under illumination is reproduced by all theoretical approaches. However, a more selective representation of the same data is the dependence of R_S on the *internal* voltage V_{int} [Fig. 5(b)]. Here, the *p-i-n* model because of its direct functional dependence of R_{int} on V_{int} as given in Eq. (13) fails to reproduce any difference between the dark and the illuminated values. The *p-n* model fits the experimental data well except for the range from $0.61\,\text{V} \leq V_{int} \leq 0.64\,\text{V}$, which corresponds to the transition range (ii) in Fig. 4 whereas the singularity of R_S at $V_{int} \approx V_{int}^{SC} \approx 604\,\text{mV}$ is even better reproduced than by the SCAPS simulations.

D. Photocurrent collection efficiency

A voltage-dependent series resistance as given in Eqs. (12) or (13) destroys basic relations that are derived from extrapolating the principle of detailed balance from the near equilibrium. The network theorem of Wong and Green [27] relates a differential modification dV_j of the

junction voltage that results from a modification dV_{ext} of the terminal voltage with the differential photocurrent collection efficiency via

$$\frac{dV_{\mathrm{int}}}{dV_{\mathrm{ext}}} = f_c^{\mathrm{ph}} := -\frac{dJ}{dJ_{\mathrm{ph}}}. \tag{18}$$

In Eq. (18), the quantity dJ is the modification of the terminal current caused by a modification dJ_{ph} of the photocurrent and the derivative defines the photocurrent collection efficiency f_c^{ph}. The standard application of the network theorem uses the fact that the local quantity $dV_j(x,y)$ is accessible as a function of the cell-surface coordinates x, y by electromodulated luminescence images. The validity of Eq. (18) then allows determination of the spatially resolved photocurrent collection efficiency $f_c^{\mathrm{ph}}(x,y)$ from luminescence images [28–32].

The equivalent circuit model shown in Fig. 2(b) is a simple zero-dimensional model such that we can replace J_{ph} by the light-generated circuit current density J_L and the junction voltage by V_{int}. As shown in Appendix B, analysis of a voltage-bias-dependent series resistance $R_S(V_{\mathrm{int}})$ yields

$$\frac{dV_{\mathrm{int}}}{dV_{\mathrm{ext}}} = \frac{1}{1 + R_S dJ/dV_{\mathrm{int}} + J dR_S/dV_{\mathrm{int}}}. \tag{19}$$

For the photocurrent collection efficiency we find

$$f_c^{\mathrm{ph}} := -\frac{dJ}{dJ_L} = \frac{1 + J dR_S/dV_{\mathrm{int}}}{1 + R_S dJ/dV_{\mathrm{int}} + J dR_S/dV_{\mathrm{int}}}. \tag{20}$$

Comparison of Eqs. (19) and (20) shows that the network theorem of Wong and Green [27] only holds with either $dR_S/dV_{\mathrm{int}} = 0$, i.e., in the absence of a bias dependence of R_S corresponding to the idea of a linear network, or at zero current bias. Note that the latter limit ($J \to 0$) ensures that the theorem is valid close to thermal equilibrium as required by the principle of detailed balance. Interestingly, a theorem closely related to the network theorem, namely the superposition of short-circuit luminescence and voltage-driven electroluminescence [15] is still valid with a bias-dependent series resistance, as shown in Appendix C.

Figure 7 demonstrates the difference between $dV_{\mathrm{int}}/dV_{\mathrm{ext}}$ and dJ/dJ_{SC}. When determining experimentally or with the SCAPS model the differential photocurrent collection efficiency via luminescence images and $dV_{\mathrm{int}}/dV_{\mathrm{ext}}$ a decrease is seen towards lower voltages. This decrease is not seen when determining dJ/dJ_{SC} directly using a small short-circuit current change (illumination change) within the SCAPS simulations. The decrease seen for $dV_{\mathrm{int}}/dV_{\mathrm{ext}}$ at low voltages under illumination results from the missing positive term JdR_S/dV_{int} in Eq. (19) (J and dR_S/dV_{int} and are both negative). Furthermore, it is seen in Fig. 7 that the experimentally determined total photocurrent collection efficiency J/J_L, which is also well reproduced by the SCAPS simulations, does not show a decrease towards lower voltages, which emphasizes that Eq. (18) leads to erroneous results for the present samples.

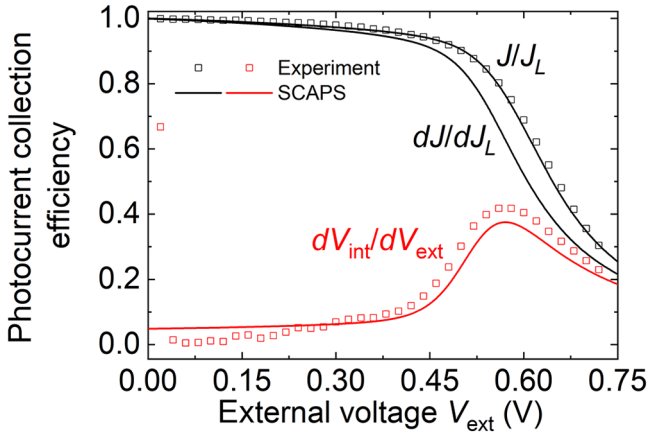

FIG. 7. Comparison of the two methods to determine the photocurrent collection efficiency. The results are found to be different in the experiment as well as the SCAPS simulations, which is in contrast to the network theorem of Wong and Green [Eq. (18)]. The photocurrent collection efficiency determined from the internal voltage is lower than the real photocurrent collection efficiency determined directly from artificially created photocurrent changes and decreases towards lower voltages. The difference is explained by a voltage-dependent series resistance, which plays a major role for the analyzed Cu(In,Ga)Se_2 samples [Eqs. (19) and (20)].

E. Loss analysis

Our numerical simulations and the modeling explain all measured data, J-V curves, and luminescence, by losses due to external and internal resistive effects. As a proof of concept, we may remove these resistive effects from the simulations by reducing the external series resistance R_{ext} to zero and/or by increasing the electron mobility μ_n to a very high number ($\mu_n = 3 \times 10^8\,\mathrm{cm^2\,V^{-1}\,s^{-1}}$), whereas keeping all other parameters constant. Figure 8 visualizes the resulting J-V curves starting with the measured data and their simulation as already shown in Fig. 6. As expected, changing R_{ext} from $3.5\,\Omega\,\mathrm{cm^2}$ to 0 yields a substantial improvement of the fill factor leaving V_{OC} and J_{SC} unchanged. On the other hand, the change from $\mu_n = 3\,\mathrm{cm^2(Vs)^{-1}}$ to $3 \times 10^8\,\mathrm{cm^2\,V^{-1}\,s^{-1}}$ (keeping R_{ext} at $3.5\,\Omega\mathrm{cm^2}$), enhances J_{SC} from 31.1 $\mathrm{mA\,cm^{-2}}$ to 31.9 $\mathrm{mA\,cm^{-2}}$.

Finally, using both changes at the same time yields a greatly improved J-V characteristics that in addition fits the experimentally determined (internal) J/V_{int} curve. The latter point highlights the consistency of our approach and proves that J/V_{int} curves determined from luminescence measurements are suitable to determine loss-free

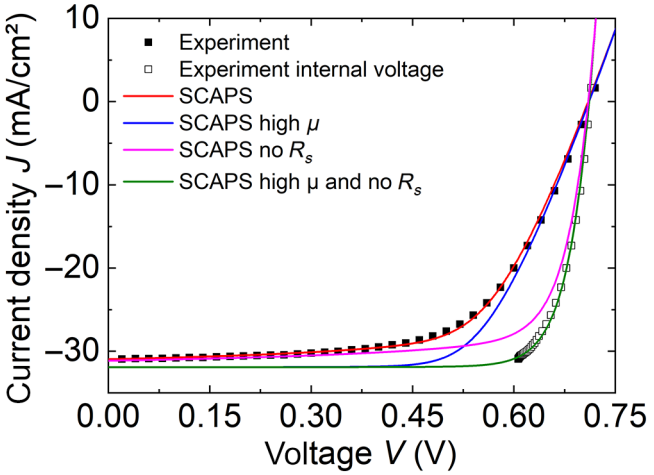

FIG. 8. Experimental J-V and J-$V_{\rm int}$ characteristics in comparison to SCAPS simulations with varying mobility and series resistance. For the high μ SCAPS simulations the electron mobility is increased from 3 to 3×10^8 cm^2/Vs and for the no R_S simulations the series resistance is set to zero. As visible, both changes improve the J-V characteristic significantly by increasing the fill factor. The increase in mobility also improves the short-circuit current. Furthermore, the J-$V_{\rm int}$ characteristics is equal to the simulated J-V characteristics with no series resistance and high mobility. Thus, the experimental J-$V_{\rm int}$ characteristic shows the whole potential of the analyzed solar cell.

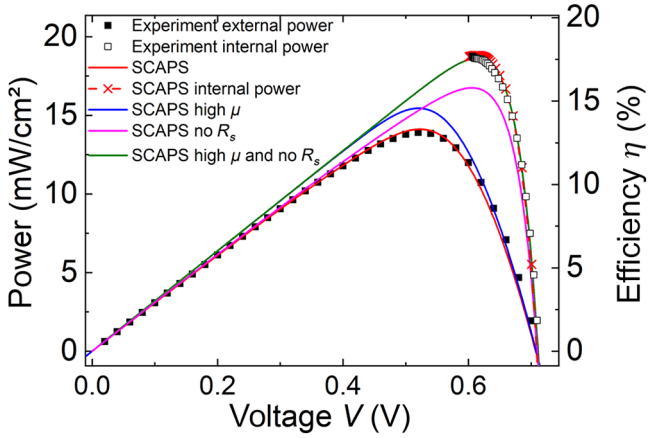

FIG. 9. Experimental power characteristics determined from the J-V and J-$V_{\rm int}$ characteristic in comparison to SCAPS simulations with varying mobility and series resistance. The power curve determined using the internal voltage is noted as internal power. For the high μ SCAPS simulations the electron mobility is increased from 3 to 3×10^8 cm^2/Vs and for the no R_S simulations the series resistance is set to zero. The increase in the mobility results in an efficiency increase of absolute 1.2%, the decrease in the series resistance results in an increase of absolute 2.4%, while an improvement of both parameters improves the efficiency by absolute 4.2%, which surpasses the sum of the individual improvements.

current-voltage curves and to determine the implied efficiency potential of a solar cell.

In order to evaluate the power losses due to external and internal resistance more closely, we plot the data from Fig. 8 in the form of power versus voltage curves by multiplying the currents with the respective voltages. Note that the efficiency axis on the right of Fig. 9 is obtained by scaling the measured output power by the ratio $J_{\rm SC}^{\rm PLsetup}/J_{\rm SC}^{\rm AM1.5} = 31.0\,{\rm mA\,cm^{-2}}/29.2\,{\rm mA\,cm^{-2}} = 1.06$ of short-circuit current measured during the luminescence measurement in the sun simulator and that measured in the sun simulator. With this correction, we have an efficiency of $\eta = 13.4\%$ (with a fill factor of FF = 64%) for the experimental data as well as for the SCAPS simulations, an efficiency of $\eta_\mu = 14.6\%$ for the simulated high mobility data, $\eta_R = 15.8\%$ for the case without external Ohmic series resistance, and $\eta_{\mu_{\rm R}} = 17.6\%$ (FF = 76%) for high mobility *and* zero series resistance. Thus, the loss due to the internal series resistance amounts to $\Delta\eta_\mu = \eta_\mu - \eta = 1.2\%$ and that of the external series resistance $\Delta\eta_R = \eta_R - \eta = 2.4\%$. The overall difference $\Delta\eta_{\mu_{\rm R}} = \eta_{\mu_{\rm R}} - \eta_{\rm exp} = 4.2\%$ between the standard model and the loss-free output efficiency contains an additional mixed term of 0.6% that results from the combined consequences of external and internal series resistance. Also shown in Fig. 9 is the fact that the simulated loss-free power curve fits the experimental internal power curve $P_{\rm int} = JV_{\rm int}$ (open squares) as well as the internal power curve obtained from simulations (crosses).

A further consistency check is given by comparing the measured ratio between the luminescence $\Phi_{\rm SC}$ under short-circuit current and $\Phi_{\rm OC}$ under open circuit with the ratio $\Delta J_{\rm SC}/J_L$. Here, the difference $\Delta J_{\rm SC} = J_L - J_{\rm SC}$ denotes the total loss of short-circuit current with respect to the total photogenerated current J_L. For the general case, including ideality factors $n_{\rm id} \neq 1$, we find

$$\frac{\Phi_{\rm SC}}{\Phi_{\rm OC}} = \left(\frac{\Delta J_{\rm SC}}{J_L}\right)^{n_{\rm id}}. \tag{21}$$

As shown in Appendix D, Eq. (21) follows from Eq. (11) for the case $n_{\rm id} = 1$ and from the approximate Eqs. (16) and (17). The luminescence ratio in our experiment is $\Phi_{\rm SC}/\Phi_{\rm OC} \approx 1.7\%$ whereas in the simulation of our experiment, we have $\Delta J_{\rm SC} = 1.4\,{\rm mA\,cm^{-2}}$ based on a total photogenerated current $J_L = 32.5\,{\rm mA\,cm^{-2}}$ and a measured short-circuit current $J_{\rm SC} = 31.1\,{\rm mA\,cm^{-2}}$. With an ideality factor $n_{\rm id} = 1.3$ we have $(\Delta J_{\rm SC}/J_L)^{n_{\rm id}} = (0.043)^{1.3} = 0.0167$ in good agreement with the measured luminescence ratio.

IV. CONCLUSIONS

The present investigations highlight the value of combined electrical and luminescence measurements under light and voltage bias for the determination of internal

as well as external resistive losses in solar cells. For the specific case of $Cu(In,Ga)Se_2$ solar cells we find a significant residual luminescence under short-circuit conditions, indicating the presence of photogenerated electron-hole pairs that are not collected by the junction. This finding also implies that the internal voltage, defined as the split between the quasi-Fermi-levels of electrons and holes, significantly differs from the external voltage at the terminals of the device. We attribute this effect to the presence of an internal series resistance, due to the transport of electrons through the space-charge region of the $Cu(In,Ga)Se_2$ absorber layer. We develop a detailed theoretical model for this effect and use this model, complemented by numerical simulations, to analyze the incomplete collection of photogenerated free charge carriers in the $Cu(In,Ga)Se_2$ solar cell and to identify the specific losses arising as a consequence of the internal and external series resistance.

From our experiments and our theoretical considerations, we conclude that residual short-circuit luminescence is not only significant for crystalline silicon solar cells with a thickness of hundreds of μm and a corresponding slow diffusion of charge carriers [12–14] but for any photovoltaic device. This is because the residual luminescence is a direct measure for the free energy loss that occurs during charge-carrier collection within any solar cell [44]. Since a finite gradient of the electrochemical potential is always necessary for the transport of charge carriers and because any split of the electrochemical potentials *must* cause externally measurable luminescence, this free energy loss should be measurable in any solar cell.

One might further look at the respective role of internal and external resistive losses as discussed here in terms of the charge-carrier separation and contact selectivity of solar cells [45]. The internal series resistance results from a *difference in electrochemical potential* corresponding to a kinetic loss as described in the selectivity model of Roe and co-workers [46]. In contrast, the external resistance results from a *difference in electrical potential* and hence is a true Ohmic resistance, as used in the contact selectivity concept of Brendel and Peibst [47]. From the present work, we conclude that both effects are present in real devices, kinetic (internal) limitations at low or zero external voltages, Ohmic (external) limitations at higher voltages. Finally, we show experimentally and theoretically that residual short-circuit luminescence leads to a violation of a basic network theorem [27] for the carrier collection in solar cells whereas the superposition of short-circuit luminescence and electroluminescence [15] is still valid.

In summary, the residual short-circuit luminescence that we describe here theoretically and experimentally should be a rather general feature of solar cells and the methodology developed should prove itself useful for a wide variety of other devices.

ACKNOWLEDGMENTS

The authors are grateful to A. Gerber and T. Kirchartz for collaboration and discussions. This work is partially supported by the Bundesministerium für Wirtschaft und Energie (BMWi) under Contracts No. 0324297 and No. 0324353.

APPENDIX A: VALIDITY OF Eqs. (16) and (17) IN THE CASE OF NONIDEAL RECOMBINATION $n_{id} \neq 1$

Since Eq. (8) is only solved analytically in the special case of an ideality factor, we use a numerical solution to derive the interdependence $V_{int}(V_{ext})$ of the internal on the external voltage. With this the external current-voltage characteristics $J(V_{ext})$ is known and the residual internal short circuit V_{int}^{SC} as well as the loss $\Delta J_{SC} = J_L - J_{SC} = J_L - J(V_{ext} = 0)$ is calculated. Note that the saturation current density J_0 for different ideality factors is calculated

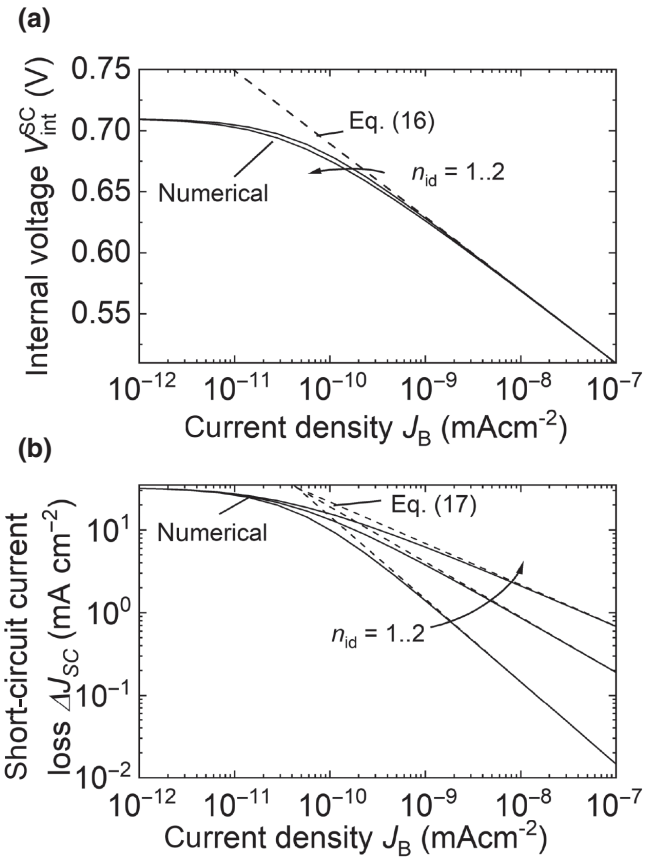

FIG. 10. (a) Dependence of the residual internal short-circuit voltage V_{int}^{SC} on the reference current density J_B for ideality factors n_{id}= 1, 1.5, and 2. (b) Dependence of the short circuit current loss ΔJ_{SC} on the reference current density J_B. The analytical approximations given by Eqs. (16) and (17) are valid for $J_B > 10^{-9}$ mA cm^{-2}.

from the fixed open-circuit voltage

$$J_0 = \frac{J_L}{\exp\left(\frac{qV_{\rm OC}}{n_{\rm id}kT}\right) - 1}. \tag{A1}$$

Figure 10 demonstrates the validity of the approximations given by Eqs. (16) and (17) for ideality factors $n_{\rm id}$ between 1 and 2 for a range of reference current densities $J_B > 10^{-9}\,{\rm mA\,cm^{-2}}$. Note that with smaller values of J_B, $V_{\rm int}^{\rm SC}$ approaches $V_{\rm OC}$ and the short-circuit current loss $\Delta J_{\rm SC}$ approaches $J_{\rm SC}$ such that the device becomes extremely poor concerning its abilities of charge-carrier separation.

APPENDIX B: VIOLATION OF THE WONG-GREEN NETWORK THEOREM

Reorganizing Eq. (15) leads to

$$V_{\rm ext} = V_{\rm int} + R_S(V_{\rm int})J. \tag{B1}$$

The derivative of Eq. (B1)

$$\frac{dV_{\rm ext}}{dV_{\rm int}} = 1 + \frac{dJ}{dV_{\rm int}}R_S + J\frac{dR_S}{dV_{\rm int}} \tag{B2}$$

leads to Eq. (19). The derivative of the terminal current J with respect to the short-circuit current J_L (under constant $V_{\rm ext}$) leads to

$$-\frac{dJ}{dJ_{\rm SC}} = 1 - \frac{dJ}{dV_{\rm int}}\frac{dV_{\rm int}}{dJ_L}. \tag{B3}$$

From Eq. (B1) we obtain

$$\frac{dV_{\rm int}}{dJ_L} = -J\frac{dR_S}{dV_{\rm int}}\frac{dV_{\rm int}}{dJ_L} - \frac{dJ}{dJ_L}R_S. \tag{B4}$$

Setting Eq. (B4) into Eq. (B3) leads to

$$-\frac{dJ}{dJ_L}\left(1 + \frac{dR_S}{dV_{\rm int}}J\right) = 1 + \frac{dR_S}{dV_{\rm int}}J + R_S\frac{dJ}{dV_{\rm int}}\frac{dJ}{dJ_L}, \tag{B5}$$

which by reorganization finally leads to Eq. (20).

APPENDIX C: SUPERPOSITION OF SHORT-CIRCUIT PHOTOLUMINESCENCE AND ELECTROLUMINESCENCE

We assume that the luminescence Φ is determined by the internal voltage $V_{\rm int}$ via the proportionality

$$\Phi \sim \left[\exp\left(\frac{qV_{\rm int}}{kT}\right) - 1\right]. \tag{C1}$$

Reorganizing Eq. (9) and the use of Eq. (C1) leads to

$$\begin{aligned}\Phi &\sim \left[\exp\left(\frac{qV_{\rm int}}{kT}\right) - 1\right] \\ &= \frac{J_B}{J_B + J_0}\left[\exp\left(\frac{qV_{\rm ext}}{kT}\right) - 1\right] + \frac{J_L}{J_B + J_0}.\end{aligned} \tag{C2}$$

With Eq. (C2) the luminescence emission is a superposition of a term that is exponentially driven by the external voltage $V_{\rm ext}$ and a residual (short-circuit) term that is driven by the photogenerated current J_L, in analogy to Ref. [15].

APPENDIX D: RATIO BETWEEN SHORT-CIRCUIT AND OPEN-CIRCUIT LUMINESCENCE

From Eq. (C2) we have under short-circuit conditions

$$\Phi_{\rm SC} \sim \frac{J_L}{J_B + J_0} \tag{D1}$$

and under open circuit

$$\begin{aligned}\Phi_{\rm OC} &\sim \frac{J_B}{J_B + J_0}\left[\exp\left(\frac{qV_{\rm ext,OC}}{kT}\right) - 1\right] + \frac{J_L}{J_B + J_0} \\ &= \frac{J_B}{J_B + J_0}\frac{J_L}{J_0} + \frac{J_L}{J_B + J_0} = \frac{(J_B + J_0)J_L}{(J_B + J_0)J_0} = \frac{J_L}{J_0}.\end{aligned} \tag{D2}$$

Thus, the ratio between short-circuit and open-circuit luminescence reads

$$\frac{\Phi_{\rm SC}}{\Phi_{\rm OC}} = \frac{J_0}{J_B + J_0}. \tag{D3}$$

Considering Eq. (11), the short-circuit current $J_{\rm SC}$ is reduced with respect to the photogenerated current by

$$\Delta J_{\rm SC} = J_L - J_{\rm SC} = J_L\left(1 - \frac{J_B}{J_0 + J_B}\right) = J_L\frac{J_0}{J_0 + J_B}. \tag{D4}$$

By comparing Eqs. (D3) and (D4) we find

$$\frac{\Phi_{\rm SC}}{\Phi_{\rm OC}} = \frac{\Delta J_{\rm SC}}{J_L}. \tag{D5}$$

Thus, the easily measurable luminescence ratio gives a direct measure for the losses in short-circuit current. Equation (D5) is however only valid if recombination follows a diode law with an ideality factor $n_{\rm id} = 1$. For

ideality factors $n_{id} \neq 1$ we find from the approximations given by Eqs. (16) and (17) the more general expression

$$\frac{\Phi_{SC}}{\Phi_{OC}} = \left(\frac{\Delta J_{SC}}{J_L}\right)^{n_{id}}. \tag{D6}$$

[1] J. Mattheis, J. H. Werner, and U. Rau, Finite mobility effects on the radiative efficiency limit of pn-junction solar cells, Phys. Rev. B **77**, 085203 (2008).

[2] W. Shockley and H. J. Queisser, Detailed balance limit of efficiency of p-n-junction solar cells, J. Appl. Phys **32**, 510 (1961).

[3] T. Fuyuki, H. Kondo, T. Yamazaki, Y. Takahashi, and Y. Uraoka, Photographic surveying of minority carrier diffusion length in polycrystalline silicon solar cells by electroluminescence, Appl. Phys. Lett **86**, 262108 (2005).

[4] T. Trupke, R. A. Bardos, M. C. Schubert, and W. Warta, Photoluminescence imaging of silicon wafers, Appl. Phys. Lett **89**, 044107 (2006).

[5] K. Bothe and D. Hinken, in *Semiconductors and Semimetals Vol. 89, Advances in Photovoltaics Vol. 2*, edited by G. P. Willeke, E. R. Weber (Academic Press, Burlington, 2013), pp. 259–339.

[6] T. Kirchartz, A. Helbig, B. E. Pieters, and U. Rau, in *Advanced Characterization Techniques for Thin Film Solar Cells*, 2nd ed., edited by D. Abou-Ras, T. Kirchartz, U. Rau (Wiley-VCH, Weinheim, Germany, 2016), pp. 61–80.

[7] A. Gerber, V. Huhn, T. M. H. Tran, M. Siegloch, B. E. Pieters, and U. Rau, Advanced large area characterization of thin-film solar modules by electroluminescence and thermography imaging techniques, Sol. Enery Mat. Sol. Cells **135**, 35 (2015).

[8] O. Breitenstein, F. Frühauf, and J. Bauer, Advanced local characterization of silicon solar cells, Phys. Status Solidi A **214**, 1700611 (2017).

[9] F. Babbe, L. Choubrac, and S. Siebentritt, The optical diode ideality factor enables fast screening of semiconductors for solar cells, Sol. RRL **2**, 1800248 (2018).

[10] U. Rau, Reciprocity relation between photovoltaic quantum efficiency and electroluminescent emission of solar cells, Phys. Rev. B **76**, 085303 (2007).

[11] P. Würfel, The chemical potential of radiation, J. Phys. C: Solid State Phys **15**, 3967 (1982).

[12] M. D. Abbott, R. A. Bardos, T. Trupke, K. Fisher, and E. Pink, The effect of diffusion-limited lifetime on implied current voltage curves based on photoluminescence data, J. Appl. Phys **102**, 044502 (2007).

[13] D. Hinken, K. Bothe, K. Ramspeck, S. Herlufsen, and R. Brendel, Determination of the effective diffusion length of silicon solar cells from photoluminescence, J. Appl. Phys **105**, 104516 (2009).

[14] M. K. Juhl and T. Trupke, The impact of voltage independent carriers on implied voltage measurements on silicon devices, J. Appl. Phys **120**, 165702 (2016).

[15] U. Rau, Superposition and reciprocity in the electroluminescence and photoluminescence of solar cells, IEEE J. Photovoltaics **2**, 169 (2012).

[16] T. Trupke, E. Pink, R. A. Bardos, and M. D. Abbott, Spatially resolved series resistance of silicon solar cells obtained from luminescence imaging, Appl. Phys. Lett **90**, 093506 (2007).

[17] D. Hinken, K. Ramspeck, K. Bothe, B. Fischer, and R. Brendel, Series resistance imaging of solar cells by voltage dependent electroluminescence, Appl. Phys. Lett **91**, 182104 (2007).

[18] O. Breitenstein, J. Bauer, D. Hinken, and K. Bothe, The reliability of thermography- and luminescence-based series resistance and saturation current density imaging, Sol. Enery Mat. Sol. Cells **137**, 50 (2015).

[19] A. Helbig, T. Kirchartz, R. Schaeffler, J. H. Werner, and U. Rau, Quantitative electroluminescence analysis of resistive losses in Cu(In,Ga)Se_2 thin-film modules, Sol. Enery Mat. Sol. Cells **94**, 979 (2010).

[20] M. Paire, L. Lombez, J.-F. Guillemoles, and D. Lincot, Measuring sheet resistance of CIGS solar cell's window layer by spatially resolved electroluminescence imaging, Thin Solid Films **519**, 7493 (2011).

[21] T. M. H. Tran, B. E. Pieters, C. Ulbrich, A. Gerber, T. Kirchartz, and U. Rau, Transient phenomena in Cu(In,Ga)Se_2 solar modules investigated by electroluminescence imaging, Thin Solid Films **535**, 307 (2013).

[22] T. M. H. Tran, B. E. Pieters, M. Schneemann, T. C. M. Müller, A. Gerber, T. Kirchartz, and U. Rau, Quantitative evaluation method for electroluminescence images of a-Si: H thin-film solar modules, Phys. Status Solidi RRL **7**, 627 (2013).

[23] T. C. M. Müller, B. E. Pieters, U. Rau, and T. Kirchartz, Analysis of the series resistance in pin-type thin-film silicon solar cells, J. Appl. Phys. **113**, 134503 (2013).

[24] U. Würfel, D. Neher, A. Spies, and S. Albrecht, Impact of charge transport on current-voltage characteristics and power-conversion efficiency of organic solar cells, Nat. Commun **6**, 6951 (2015).

[25] O. Breitenstein, An alternative one-diode model for illuminated solar cells, IEEE J. Photovolt. **4**, 899 (2014).

[26] O. Breitenstein, An alternative one-diode model for illuminated solar cells, Energy Procedia **55**, 30 (2014).

[27] J. Wong and M. A. Green, From junction to terminal: Extended reciprocity relations in solar cell operation, Phys. Rev. B **85**, 235205 (2012).

[28] U. Rau, V. Huhn, L. Stoicescu, M. Schneemann, Y. Augarten, A. Gerber, and B. E. Pieters, Photocurrent collection efficiency mapping of a silicon solar cell by a differential luminescence imaging technique, Appl. Phys. Lett **105**, 163507 (2014).

[29] J. Wong, R. Sridharan, Y. C. Wang, and T. Mueller, in *IEEE 40th Photovoltaic Specialist Conference (PVSC)*, Denver, CO, (2014), pp. 975.

[30] A. Delamarre, L. Lombez, K. Watanabe, M. Sugiyama, Y. Nakano, and J. F. Guillemoles, Experimental demonstration of optically determined solar cell current transport efficiency map, IEEE J. Photovolt. **6**, 528 (2016).

[31] V. Huhn, A. Gerber, Y. Augarten, B. E. Pieters, and U. Rau, Analysis of Cu(In,Ga)Se_2 thin-film modules by electro-modulated luminescence, J. Appl. Phys. **119**, 095704 (2016).

[32] V. Huhn, B. E. Pieters, Y. Augarten, A. Gerber, D. Hinken, and U. Rau, Imaging photocurrent collection losses in solar cells, Appl. Phys. Lett **109**, 223502 (2016).

[33] S. M. Sze and K. K. Ng, *'Physics of Semiconductor Devices'* (John Wiley and Sons, Hoboken, NJ, 2007), pp. 85–91.

[34] B. Dimmler and R. Wächter, Manufacturing and application of CIS solar modules, Thin Solid Films **515**, 5973 (2007).

[35] M. Burgelman, P. Nollet, and S. Degrave, Modelling polycrystalline semiconductor solar cells, Thin Solid Films **361-362**, 527 (2000).

[36] J. F. L. Salas, S. J. Heise, M. Richter, V. Gerliz, M. S. Hammer, J. Ohland, and I. Hammer-Riedel, Simulation of metastable changes in time resolved photoluminescence of Cu(In,Ga)Se_2 thin film solar cells upon light soaking treatment, Thin Solid Films **633**, 40 (2016).

[37] S. J. Heise, V. Gerliz, M. S. Hammer, J. Ohland, J. Keller, and I. Hammer-Riedel, Light-induced changes in the minority carrier diffusion length of Cu(In,Ga)Se_2 absorber material, Sol. Enery Mat. Sol. Cells **163**, 270 (2017).

[38] Supplemental Material at http://link.aps.org/supplemental/10.1103/PhysRevApplied.14.014046 for SCAPS Simulation parameters.

[39] T. Kirchartz, U. Rau, M. Hermle, A. W. Bett, A. Helbig, and J. H. Werner, Internal voltages in GaInP/GaInAs/Ge multijunction solar cells determined by electroluminescence measurements, Appl. Phys. Lett **92**, 123502 (2008).

[40] J. H. Werner, J. Mattheis, and U. Rau, Efficiency limitations of polycrystalline thin film solar cells: Case of Cu(In,Ga)Se_2, Thin Solid Films **480–481**, 399 (2005).

[41] J. Mattheis, U. Rau, and J. H. Werner, Light absorption and emission in semiconductors with band gap fluctuations - A study on Cu(In,Ga)Se_2 thin films, J. Appl. Phys. **101**, 113519 (2007).

[42] D. Abou-Ras, N. Schäfer, C. J. Hages, S. Levenko, J. Marquez, and T. Unold, Inhomogeneities in Cu(In,Ga)Se_2 thin films for solar cells: Band-gap versus potential fluctuations, Solar RRL **2**, 1700199 (2018).

[43] J. P. Teixeira, P. M. P. Salomé, B. Alves, M. Edoff, and J. P. Leitão, Evidence of Limiting Effects of Fluctuating Potentials on VOC of Cu(In,Ga)Se_2 Thin-Film Solar Cells, Phys. Rev. Appl. **11**, 054013 (2019).

[44] R. Brendel, S. Dreissigacker, N.-P.- Harder, and P. P. Altermatt, Theory of analyzing free energy losses in solar cells, Appl. Phys. Lett **93**, 173503 (2008).

[45] U. Rau and T. Kirchartz, Charge carrier collection and contact selectivity in solar cells, Adv. Mat. Interf **6**, 1900252 (2019).

[46] E. T. Roe, K. E. Egelhofer, and M. C. Lonergan, Limits of contact selectivity/recombination on the open-circuit voltage of a photovoltaic, ACS Appl. Energy Mater **1**, 1037 (2018).

[47] R. Brendel and R. Peibst, Contact selectivity and efficiency in crystalline silicon photovoltaics, IEEE J. Photovolt. **6**, 1413 (2016).